

Large non-collinearity and spin-reorientation in the novel Mn_2RhSn Heusler magnet

O. Meshcheriakova^{1,2}, S. Chadov², A. K. Nayak², U. K. Rößler³, J. Kübler⁴, G. André⁵,
A. A. Tsirlin², J. Kiss², S. Hausdorf², A. Kalache², W. Schnelle², M. Nicklas², C. Felser²

¹*Graduate School of Excellence "Materials Science in Mainz" Johannes Gutenberg - Universität, 55099 Mainz, Germany*

²*Max-Planck-Institut für Chemische Physik fester Stoffe, Nöthnitzer Str. 40, 01187 Dresden, Germany*

³*Leibniz-Institut für Festkörper- und Werkstoffforschung IFW, Helmholtz Str. 20, 01171 Dresden, Germany*

⁴*Institut für Festkörperphysik, Technische Universität Darmstadt, Germany and*

⁵*Laboratoire Léon Brillouin, CEA-CNRS Saclay, Gif-sur-Yvette Cedex, France*

Non-collinear magnets provide essential ingredients for the next generation memory technology. It is a new prospect for the Heusler materials, already well-known due to the diverse range of other fundamental characteristics. Here we present combined experimental/theoretical study of novel non-collinear tetragonal Mn_2RhSn Heusler material exhibiting unusually strong canting of its magnetic sublattices. It undergoes a spin-reorientation transition, induced by a temperature change and suppressed by an external magnetic field. Due to the presence of Dzyaloshinskii-Moriya exchange and magnetic anisotropy, Mn_2RhSn is suggested to be a promising candidate for realizing the skyrmion state in the Heusler family.

The art of controlling magnetic degrees of freedom has led to a broad range of applications that make up the rapidly developing field of spintronics. Up to now, most of the exploited compounds have been so-called collinear magnets, i.e. materials in which the magnetization is formed by local magnetic moments aligned parallel or antiparallel to one another. Yet, the possibility of influencing their mutual orientation opens new horizons for the field of spintronics. Non-collinear magnets can be widely applied in current-induced spin-dynamics [1], magnetic tunnel junctions [2], molecular spintronics [3], spin-torque transfer by small switching currents [4] and anomalous exchange bias [5]. Impressive improvement of the critical current density by five orders of magnitude [6–8] is offered by non-collinear magnets driven into the skyrmion phase [6–14]. While such exotic magnetic arrangements are sensitive to external conditions (magnetic field and temperature), an expansion of the related material base is important for their stabilization.

Flexible tuning of the magnetic properties can ultimately be realized in multicomponent systems of several magnetic sublattices with competing types of interactions such as magneto-crystalline anisotropy, dipole-dipole and Dzyaloshinsky-Moriya (DM) interactions [15, 16]. Heusler compounds, of which there are over 1000 members, provide a rich variety of parameters for almost any material engineering task (e.g. half-metallic ferromagnetism [17, 18], shape memory [19], exchange bias [20], topological insulators [21], spin-gapless semiconductivity [22], spin-resolved electron localization [23] and superconductivity [24]). Furthermore, the majority of Mn_2YZ (Y – transition metal, Z – main-group atom) systems are non-centrosymmetric; this together with the magneto-crystalline anisotropy induced by intrinsic tetragonal distortion makes such systems attractive for skyrmion research.

First, we will discuss here the unusual ground-state magnetic canting observed in Mn_2RhSn together with

the subsequent temperature-induced spin-reorientation into the collinear ferrimagnetic mode. Further, we will give a detailed micromagnetic analysis which suggests this collinear regime to provide perfect conditions for the skyrmion formation, in agreement with the earlier theoretical studies [9, 25, 26].

In a non-relativistic case, the magnetic non-collinearity is a result of the competition between antiparallel and parallel exchange interactions (or between several types of antiparallel interactions). Such a situation is often encountered in Mn_2YZ compounds, but not all of them exhibit non-collinearity. In general, these materials crystallize in the non-centrosymmetric $\bar{1}4m2$ structure with two non-equivalent Wyckoff positions occupied by Mn atoms: Mn_I at $2b$ ($0, 1/2, 0$) and Mn_II at $2d$ ($0, 1/2, 3/4$). Z and Y elements occupy the $2a$ ($0, 0, 0$) and $2c$ ($0, 1/2, 1/4$) positions, respectively (Fig. 1a). The most significant exchange coupling between the nearest Mn_I and Mn_II atoms is characterized by a large exchange constant ($J_{\text{Mn}_\text{I}-\text{Mn}_\text{II}} \sim -20$ meV) (e.g. [27]) that leads to a typical collinear FiM (ferrimagnetic) state. Despite the fact that the in-plane interaction of Mn atoms can be rather complicated (e.g. the nearest in-plane neighbours couple parallel, the next-nearest couple antiparallel or parallel, and so on), these interactions are rather weak compared to $J_{\text{Mn}_\text{I}-\text{Mn}_\text{II}}$, which always aligns the Mn spin moments of the same plane parallel to one another (Fig. 1b). For this reason, we initially do not consider the in-plane interactions but will expand the description in terms of the effective *inter-plane* exchange coupling J , which indicates the interaction of a certain Mn atom (i) with all other Mn atoms (i') in a different plane, i.e. $J = \sum_{i'} J_{ii'}$.

Since the collinear order being substantially determined by the nearest-plane J interaction becomes even more stable if the Y atom is magnetic (as e.g. in case of Mn_2CoZ systems [27]), our further consideration concerns Mn_2YZ Heusler materials with the non-magnetic heavy Y elements (such as Rh or Ir, since in case of

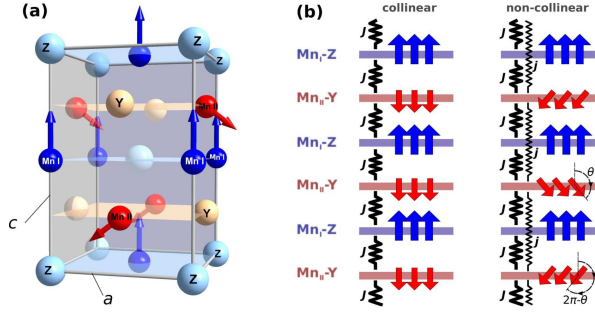


FIG. 1. (a) Crystal and magnetic structures of Mn₂YZ Heusler compounds. Due to the magneto-crystalline anisotropy induced by the tetragonal distortion, the Mn_I magnetic moments are oriented along the c axis; the moments on Mn_{II} are canted in an alternating manner with respect to the c axis. (b) Schematic picture of the leading magnetic exchange interactions between different atomic layers in Mn₂YZ (atomic planes containing Z and Y elements are shown in blue and red, respectively). The arrows show the orientation of the spin moments on Mn and the springs show the exchange interactions between different planes. Considering only the nearest antiparallel interactions J (between Mn_I-Z and Mn_{II}-Y planes) leaves the magnetic structure collinear; introducing the next-nearest antiparallel coupling j (between Mn_{II}-Y planes) leads to the alternating canting of Mn_{II} moments by θ and $2\pi - \theta$.

light elements, such as Ti or V, Mn atoms occupy equivalent $2c$ and $2d$ positions). In this case, the collinearity can be perturbed by the next important interaction j between the next-nearest planes, e.g. between pairs of Mn_{II}-Y planes as shown in Fig. 1b. This interaction is antiparallel due to its indirect origin realized through the main-group element Z (super-exchange) [28]. Since j tends to rotate the moments of the nearest Mn_{II}-Y planes antiparallel to each other, it competes with the strong antiparallel exchange J , and may then result in a non-trivial canting angle ($\theta \neq 0^\circ, 180^\circ$, Fig. 1b). The relevant θ -dependent part of the Heisenberg Hamiltonian will contain only antiparallel interactions:

$$H_\theta = -J \cos \theta - \frac{1}{2} \cdot j \cos 2(\pi - \theta), \quad (1)$$

where the first term is the coupling of the nearest planes (Mn_I-Z with Mn_{II}-Y) and the second is that of the next-nearest (Mn_{II}-Y) planes. The factor $1/2$ accounts for the twice sparser entrance of the next-nearest plane couplings. The extrema of H_θ are found from:

$$\sin \theta \left(\frac{1}{2} + \frac{j}{J} \cos \theta \right) = 0, \quad (2)$$

and $\theta_{1,2} = 180^\circ \pm \arccos \left(\frac{J}{2j} \right)$ non-collinear solutions are given subject to the condition $j/J > 1/2$, which means that the canting occurs only if the next-nearest antiparallel exchange j is sufficiently strong.

To justify the proposed magnetic order we performed *ab initio* calculations (Supporting Information [31],

Mn ₂ YZ	m_{MnI}	m_{MnII}	$\theta_{1,2} [^\circ]$	m_Y	M	M_{exp}
Mn ₂ RhSn	3.51	3.08	180 ± 55	0.14	1.9	1.97
Mn ₂ PtIn	3.38	3.30	180 ± 50	0.12	1.4	1.6
Mn ₂ IrSn	3.52	3.08	180 ± 44	0.09	1.4	1.5

TABLE I. Computed atomic magnetic moments m , canting angles $\theta_{1,2}$ and total magnetization per formula unit $M = m_{\text{MnI}} + m_{\text{MnII}} \cdot \cos \theta + m_Y$, compared to the experimentally measured magnetization M_{exp} . Values of magnetic moments/magnetization are given in μ_B .

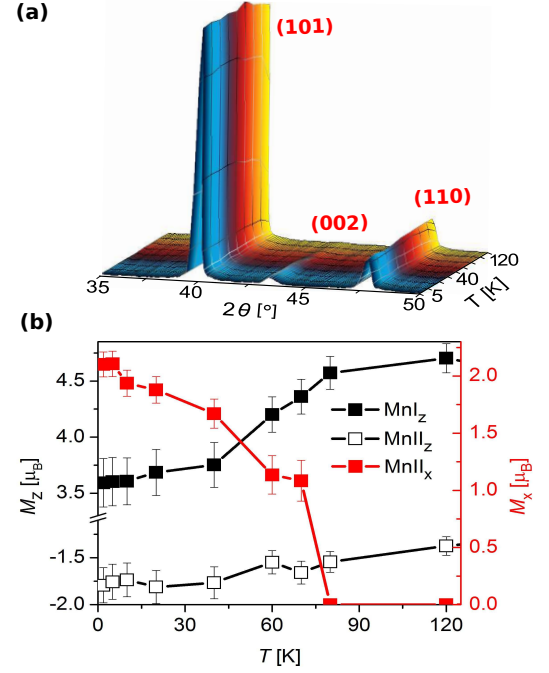


FIG. 2. (a) Temperature-dependent neutron diffraction spectra. The (002)-peak decays over 1.8-80 K. (b) Weakening of the in-plane magnetism (produced by Mn_{II} x -component) releases the z -component of Mn_I, while the z -component of Mn_{II} evolves rather insignificantly.

Sec. V) for Mn₂RhSn and another two similar Heusler systems, Mn₂PtIn and Mn₂IrSn. For Mn₂RhSn, the plot of the total energy as a function of θ indeed exhibits two energy minima corresponding to the non-trivial canting angles $\theta_{1,2} = 180^\circ \pm 55^\circ$. Similar plots were obtained for another two compounds (Supporting Information [31], Fig. S8). Calculated local moments, their orientations, total magnetization, and experimentally measured one, are summarized in Tab. I. These magnetic properties may be significantly affected by those kinds of disorder which are typical for Heusler systems. The details of this aspect are discussed in Supporting Information [31] (Sec. IV).

Powder neutron scattering data convincingly demonstrate the predicted ground-state non-collinearity (Fig. 2). At 1.8 K the magnetic moments are 3.59 and 3.47 μ_B on Mn_I and Mn_{II}. The value obtained for the more localized Mn_I correlates with the calculated result

(Tab. I), while the Mn_{II} moment is larger: it is defined less precisely as the scattering events on itinerant moments are more dispersed. The magnetic structure was found to be canted by about $\theta_{1,2} = (180 \pm 58.9)^\circ$ within alternating Mn_{II} -Rh planes. It is important to note, that such strong magnetic canting was never reported for the Heusler materials, in which it is typically of an order few degrees at most.

Being non-collinear in the ground state, the magnetic configuration evolves with changes to the temperature and external field. Observation of the (002)-peak intensity for $T \leq 80$ K indicates the presence of in-plane magnetism (Fig. 2b). As the temperature increases, the peak gradually decreases and subsequently vanishes for $T > 80$ K, suggesting that the in-plane magnetic component is suppressed (Fig. 2b). This is attributed to the gradual spin-reorientation of the Mn_{II} sublattice; the canting angle decreases until a collinear FiM order sets in at 80 K. Such behavior is strongly pronounced in the $M(T)$ curves measured in weak fields (0.1-0.5 T, Fig. 3a) and suppressed in stronger fields (5 T). This is evidently an intrinsic effect as the applied fields are larger than the coercive field ($H_c = 0.065$ T). It is not only the mutual orientation of the site-specific moments that changes but their absolute values also change (Fig. 3c). In the canted lowest-temperature state, the Mn_{I} moment is somewhat compensated by the equally strong Mn_{II} . As the temperature increases, the moments of Mn_{II} delocalize further and release the Mn_{I} to reach $4.5 \mu_B$. This occurs gradually, and the slope of the zero-field heat capacity curve changes (Fig. 3e); the spin-wave term is sufficiently weak in comparison to the electronic and phonon contributions that no sharp anomaly is visible. However, the onset of the FiM phase is characterized by the explicit step-like increase in the ac-susceptibility signal (Fig. 3b). Measured values of χ' and χ'' were found to be independent of the frequency, suggesting a high magnetic homogeneity. The evolution of the magnetism with temperature is echoed by the crystal structure (Fig. 3f). Although the a -parameter increases monotonically, the change in c -parameter is non-linear and corresponds to the ac-susceptibility behavior. The sudden rise in the vicinity of 280 K is an anomaly corresponding to T_C . The c -parameter eventually decreases until a transition to the cubic phase occurs at about 570°C (Supporting Information [31], Fig. S5).

By systematic coarse-graining of the spin-lattice model a micromagnetic continuum theory has been developed (Supporting Information [31], Sec. VI). Considering only the leading Heisenberg-like exchange, the analysis shows that in tetragonal inverse Mn_2YZ Heusler alloys, the magnetic ordering displays coexisting magnetic modes with ferrimagnetism (FiM) of the two sublattices and an antiferromagnetic mode (AFM) on the Mn_{II} -sublattice. These systems, thus, are close to a bicritical (or tetracritical) point in their magnetic phase diagram. In

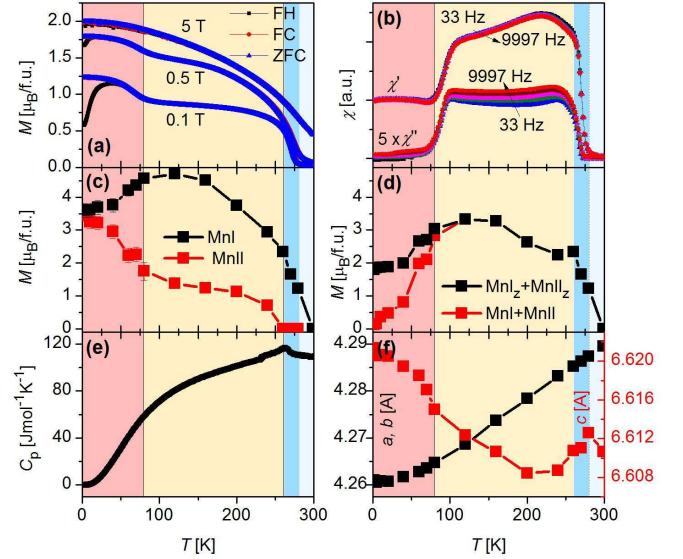


FIG. 3. Evolution of the magnetic structure with the temperature. Canted (red), collinear ferrimagnetic (yellow) and disordered (blue) magnetic states of Mn_2RhSn . (a) Zero-field-cooled (ZFC), field-cooled (FC) and field-heated (FH) magnetization as a function of the temperature measured at induction fields of 0.1, 0.5, and 5 T. (b) Real (χ') and imaginary (χ'') ac-susceptibility components are frequency independent and show a pronounced step at the onset of the FiM phase. (c) The change in the canting angle occurs because of the simultaneous re-alignment of the Mn_{II} moment and a decrease in its absolute value. This, in turn, releases the previously suppressed Mn_{I} moment from 3.5 to $4.5 \mu_B$. (d) The sum of the total and z -components of the $\text{Mn}_{\text{I(II)}}$ moments follows the ac-susceptibility behavior. No in-plane component is present after 80 K. (e) A change in the slope of the heat capacity curve is observed in the vicinity of the spin-reorientation. (f) Evolution of the lattice parameters with temperature: the change in the magnetism is echoed mainly by the c -parameter, while a evolves monotonically.

Mn_2RhSn , the thermodynamic potential favours a dominating collinear FiM order for $T > 80$ K. Below this temperature the AFM sets in. By the crystal symmetry of Mn_2YZ , *chiral inhomogeneous DM couplings* exist in spatial directions perpendicular to the crystal axis [25, 26] that cause a spiral twist of these magnetic modes with long pitch. The micromagnetic model for the FiM state is exactly the Dzyaloshinskii-model for a magnetic order in acentric tetragonal crystals from $\bar{4}2m$ (D_{2d}) class [25, 29]. Therefore, in the collinear FiM state, chiral skyrmions and skyrmion lattices exist in these magnets, as predicted in Ref. [9, 25]. The micromagnetic model predicts a chiral twisting length $\Lambda \sim 130$ nm, which corresponds to the diameter of the FiM-state skyrmions. These chiral skyrmion states exist in the inverse Heusler alloys without the need of any additional effects not accounted for by the basic magnetic couplings, i.e. Heisenberg-like and DM-exchange and leading anisotropies, and at arbitrary temperature.

This is in contrast to chiral cubic helimagnets, which require fine-tuned additional effects for the existence of skyrmionic states. Because the tetragonal lattice also induces a sizeable easy-axis magneto-crystalline anisotropy in Mn_2RhSn , as calculated by relativistic DFT, the magnetic phase diagram is not expected to display a field-driven condensed skyrmion phase in this FiM-state. The ratio of easy-axis anisotropy to DM coupling is large. Using the universal phase diagram of chiral magnets [9], skyrmions do exist as nonlinear solitonic excitations of the collinear state in Mn_2RhSn . Therefore, this inverse Heusler alloy is an ideal system to realize reconfigurable nanomagnetic patterns composed of its two-dimensional free skyrmions at elevated temperatures.

Coexistence of FiM and AFM orders in the canted state will be the subject to different DM-couplings. Thus, in the ground-state, novel types of chirally twisted textures can exist in Mn_2YZ alloys. These chiral DM-couplings favour different twisting lengths for the two modes and their interaction. Then, the magnetic order may become quasiperiodic and exceedingly complex, as recently described for the similar case of textures in biaxial nematic liquid crystals [30]. The presence of several DM-terms and anisotropies affecting the coexisting magnetic modes promise a rich behavior of chiral textures in tetragonal inverse Heusler alloys Mn_2YZ . E.g., closely below the onset of spin-reorientation temperature, the chiral skyrmion of the FiM-state is superimposed by a vortex-like AFM-configuration on the Mn_{II} -sublattice with a defect in the core of the soliton configuration. In the ground-state, such configurations may become unstable, depending on the stiffness of the AFM order. Up to now, such complex configurations have been analysed only for the simpler case of chiral AFMs with a coexisting weak-FM mode [26].

As we have demonstrated theoretically and experimentally, the design of non-collinear magnets within the Heusler family of materials can be based on Mn_2YZ compositions, with Y and Z being a non- or weakly-magnetic transition-metal and a main-group element, respectively. The choice of the Mn_2YZ Heusler group allows to control the canting angles by, e.g. combining the Y and Z elements or varying the Mn content. The use of heavy transition metals (e.g. as in the present case, $\text{Y}=\text{Pt}$, Rh , Ir and $\text{Z}=\text{Sn}$, In) amplifies the magnetically-relevant relativistic effects that are already present in these systems, such as the DM interaction and magneto-crystalline anisotropy. Such multiple magnetic degrees of freedom together with the possibility of their manipulation provided by the family of Mn_2YZ Heusler materials is vital for efficient engineering and stabilization of various magnetic orders. In particular, Mn_2RhSn is suggested to be a promising candidate for realizing the skyrmion state in the Heusler family.

Authors thank A. Bogdanov, R. Stinshoff and A. Beleanu for helpful discussions. The support of the Euro-

pean Commission under the 7th Framework Programme: Integrated Infrastructure Initiative for Neutron Scattering and Muon Spectroscopy: NMI3-II/FP7 - Contract No. 283883, the Graduate School of Excellence 'Materials Science in Mainz', the DFG project FOR 1464 'ASPI-MATT' and the European Research Council (ERC) for 'Idea Heusler!' are gratefully acknowledged.

-
- [1] P. Baláz, M. Gmitra, and J. Barnaś, *Phys. Rev. B* **80**, 174404 (2009)
 - [2] Y. Miura, K. Abe, and M. Shirai, *Phys. Rev. B* **83**, 214411 (2011)
 - [3] A. Soncini and L. F. Chibotaru, *Phys. Rev. B* **81**, 132403 (2010)
 - [4] N. L. Chung, M. B. A. Jalil, S. G. Tan, J. Guo, and S. B. Kumar, *J. Appl. Physics* **104**, 084502 (2008)
 - [5] Y. F. Tian, J. F. Ding, W. N. Lin, Z. H. Chen, A. David, M. He, W. J. Hu, L. Chen, and T. Wu, *Sci. Reports* **3**, 1094 (2013)
 - [6] F. Jonietz, S. Mühlbauer, C. Pfleiderer, A. Neubauer, W. Münzer, A. Bauer, T. Adams, R. Georgii, P. Böni, R. A. Duine, K. Everschor, M. Garst, and A. Rosch, *Science* **330**, 1648 (2010)
 - [7] X. Z. Yu, N. Kanazawa, W. Z. Zhang, T. Nagai, T. Hara, K. Kimoto, Y. Matsui, Y. Onose, and Y. Tokura, *Nature Communications* **3** (2012)
 - [8] T. Schulz, R. Ritz, A. Bauer, M. Halder, M. Wagner, C. Franz, C. Pfleiderer, K. Everschor, M. Garst, and A. Rosch, *Nat. Phys.* **8**, 301 (2012)
 - [9] A. N. Bogdanov and A. Hubert, *J. Magn. Magn. Materials* **138**, 255 (1994)
 - [10] S. Mühlbauer, B. Binz, F. Jonietz, C. Pfleiderer, A. Rosch, A. Neubauer, R. Georgii, and P. Böni, *Science* **323**, 915 (2009)
 - [11] U. K. Rößler, A. N. Bogdanov, and C. Pfleiderer, *Nature* **442**, 797 (2006)
 - [12] S. Seki, X. Z. Yu, S. Ishiwata, and Y. Tokura, *Science* **336**, 198 (2012)
 - [13] X. Yu, M. Mostovoy, Y. Tokunaga, W. Zhang, Y. M. Koji Kimoto, Y. Kaneko, N. Nagaosa, and Y. Tokura, *PNAS* **109**, 8856 (2012)
 - [14] P. Milde, D. Köhler, J. Seidel, L. M. Eng, A. Bauer, A. Chacon, J. Kindervater, S. Mühlbauer, C. Pfleiderer, S. Buhandt, C. Schütte, and A. Rosch, *Science* **340**, 1076 (2013)
 - [15] I. Dzyaloshinsky, *J. Phys. Chem. Solids* **4**, 241 (1958)
 - [16] T. Moriya, *Phys. Rev.* **120**, 91 (1960)
 - [17] J. Kübler, A. R. Williams, and C. B. Sommers, *Phys. Rev. B* **28**, 1745 (1983)
 - [18] R. A. de Groot, F. M. Mueller, P. G. van Engen, and K. H. J. Buschow, *Phys. Rev. Lett.* **50**, 2024 (1983)
 - [19] R. Kainuma, Y. Imano, W. Ito, Y. Sutou, H. Morito, S. Okamoto, O. Kitakami, K. Oikawa, A. Fujita, T. Kanomata, and K. Ishida, *Nature* **439**, 957 (2006)
 - [20] A. K. Nayak, M. Nicklas, S. Chadov, C. Shekhar, Y. Skourski, J. Winterlik, and C. Felser, *Phys. Rev. Lett.* **110**, 127204 (2013)
 - [21] S. Chadov, X.-L. Qi, J. Kübler, G. H. Fecher, C. Felser, and S.-C. Zhang, *Nature Materials* **9**, 541 (2010)

- [22] S. Ouardi, G. H. Fecher, C. Felser, and J. Kübler, Phys. Rev. Lett. **110**, 100401 (2013)
- [23] S. Chadov, J. Kiss, and C. Felser, Adv. Func. Mater. **23**, 832 (2013)
- [24] T. Klimczuk, C. H. Wang, K. Gofryk, F. Ronning, J. Winterlik, G. H. Fecher, J.-C. Griveau, E. Colineau, C. Felser, J. D. Thompson, D. J. Safarik, and R. J. Cava, Phys. Rev. B **85**, 174505 (2012)
- [25] A. N. Bogdanov and D. A. Yablonskii, Sov. JETP **68**, 101 (1989)
- [26] A. N. Bogdanov, U. K. Rössler, M. Wolf, and K.-H. Müller, Phys. Rev. B **66**, 214410 (2002)
- [27] M. Meinert, J.-M. Schmalhorst, and G. Reiss, J. Phys.: Condens. Matter **23**, 116005 (2011)
- [28] H.-B. Luo, Q.-M. Hu, C.-M. Li, B. Johansson, L. Vitos, and R. Yang, J. Phys.: Condens. Matter **25**, 156003 (2013)
- [29] I. E. Dzyaloshinskii, Sov. Phys. JETP **19**, 960 (1964)
- [30] V. L. Golo, E. I. Kats, A. A. Sevenyuk, and D. O. Sinit-syn, Phys. Rev. E **88**, 042504 (2013)
- [31] See Supporting Information [URL], which includes Refs. [32-39]
- [32] J. Rodríguez-Carvajal, *FULLPROF computer program*, LLB, Saclay (2004), version 2.80
- [33] V. Alijani, O. Meshcheriakova, J. Winterlik, G. Kreiner, G. H. Fecher, and C. Felser, J. Appl. Physics **113**, 063904 (2013)
- [34] A. K. Nayak, C. Shekhar, J. Winterlik, A. Gupta, and C. Felser, Appl. Phys. Lett. **100**, 152404 (2012)
- [35] J. Kiss, S. Chadov, G. H. Fecher, and C. Felser, Phys. Rev. B **87**, 224403 (2013)
- [36] H. Ebert, D. Ködderitzsch, and J. Minár, Rep. Prog. Phys. **74**, 096501 (2011)
- [37] S. H. Vosko, L. Wilk, and M. Nusair, Can. J. Phys. **58**, 1200 (1980)
- [38] A. I. Liechtenstein, M. I. Katsnelson, V. P. Antropov, and V. A. Gubanov, J. Magn. Magn. Materials **67**, 65 (1987)
- [39] H. Ebert and S. Mankovsky, Phys. Rev. B **79**, 045209 (2009)

Supplemental: Large Noncollinearity and Spin Reorientation in Novel Mn_2RhSn Heusler Magnet

O. Meshcheriakova,^{1,2} S. Chadov,² A. K. Nayak,² U. K. Rößler,³ J. Kübler,⁴ G. André,⁵

A. A. Tsirlin,² J. Kiss,² S. Hausdorf,² A. Kalache,² W. Schnelle,² M. Nicklas,² and C. Felser²

¹Graduate School of Excellence "Materials Science in Mainz" Johannes Gutenberg - Universität, 55099 Mainz, Germany

²Max-Planck-Institut für Chemische Physik fester Stoffe,
Nöthnitzer Strasse 40, 01187 Dresden, Germany

³Leibniz-Institut für Festkörper- und Werkstoffforschung IFW, Helmholtz Strasse 20, 01171 Dresden, Germany

⁴Institut für Festkörperphysik, Technische Universität Darmstadt, 64289 Darmstadt, Germany and

⁵Laboratoire Lon Brillouin, CEA-CNRS Saclay, 91191 Gif-sur-Yvette Cedex, France

I. SYNTHESIS OF Mn_2RhSn AND Mn_2IrSn

Polycrystalline samples were repeatedly arc-melted from stoichiometric amounts of high-purity commercially available elements in an Ar atmosphere with an overall mass loss of less than 0.5 wt.%. In each melting run, a piece of titanium was used to purify the residual atmosphere. A two-step process was employed for Mn_2RhSn : a premelt of Rh-Sn was prepared, and this was then placed on the Mn. According to the respective phase diagrams, Rh and Sn react well with each other and form a stable phase. In the second step, when the premelt is heated, it absorbs the Mn pieces, and the evaporation of Mn is minimized. To ensure homogeneity, the samples were melted 3 times on each side. As a result, after the Mn is absorbed by the phase, evaporation of the complete phase, not the single elements, takes place.

The Mn_2IrSn sample was prepared by induction heating. The procedure was repeated several times to ensure homogeneity: six repetitions of arc-melting and two of induction heat. In the latter process, the sample was maintained in the liquid state for 5 min. After 1 week of annealing, the arc-melted samples were fast cooled, whereas the induction-heated samples were cooled slowly. The ingots were then wrapped in Ta foil and annealed in evacuated silica tubes at 800°C for 1 week. To reduce the amount of surface oxidation, Mn pieces were preliminary sealed in evacuated silica tubes and left overnight at 900°C for purification. These pieces were processed repeatedly until a shiny silver-coloured surface was obtained.

II. PRIOR CHARACTERIZATION

Metallographic analysis by scanning electron (Fig. S1) and optical (Fig. S2) microscopy revealed that the samples are single-phase materials with a homogeneous composition distribution. The composition was characterized by energy-dispersive X-ray (EDX) spectroscopy (values are summarized in Tab. S1). Since the electron penetration depth is on the order of nanometres, a well-polished sample surface is essential for eliminating morphology effects. For this reason, the samples were embedded in epoxy resin blocks, and a smooth surface was prepared.

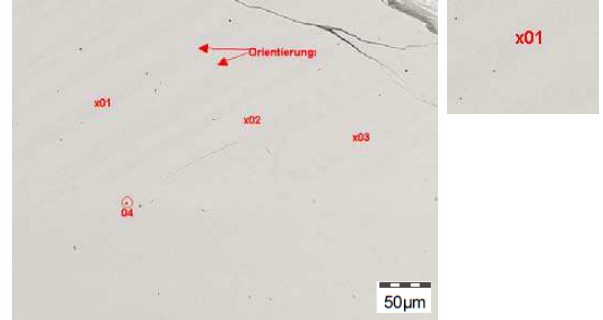


FIG. S1. SEM image of Mn_2RhSn ; composition analysis was performed at the areas marked. The Mn_2RhSn stoichiometry is constant across the whole sample; a minor impurity of $\text{Mn}_{3.5}\text{RhSn}$ is present at around 1 at.% and does not bias the presented results.



FIG. S2. An optical microscope image of the homogeneous Mn_2RhSn phase.

The measured composition deviates from the target values by 0.5 at.%, which is within the range of experimental error.

A. X-ray diffraction

Powder X-ray diffraction patterns (Fig. S3) were ob-

Spot	Mn (at.%)	Rh (at.%)	Sn (at.%)
1)	49.73	25.55	24.71
2)	48.79	25.73	25.48
3)	47.84	26.23	25.93

TABLE S1. EDX analysis of the Mn_2RhSn sample taken from the areas indicated in Fig. S1. The composition is well reproduced across the whole observed area.

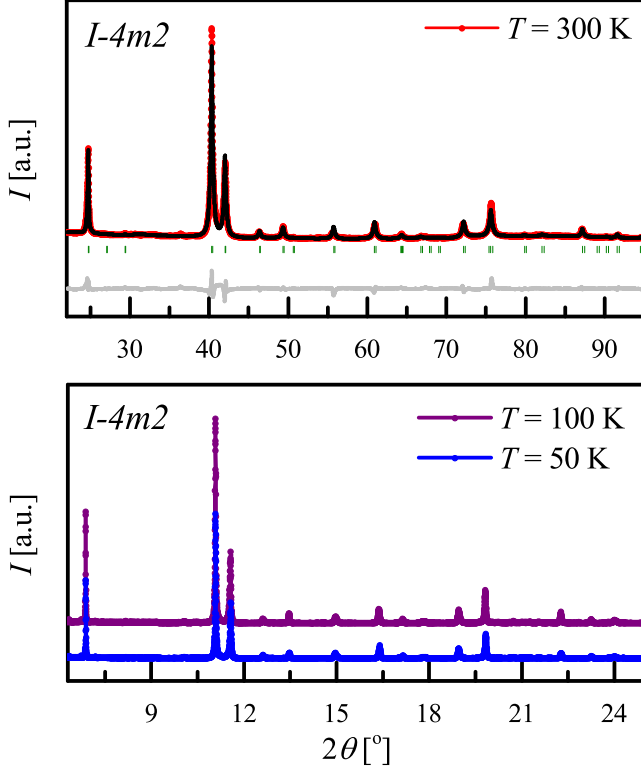


FIG. S3. Powder X-ray patterns obtained at room temperature (top) and 50 and 100 K (bottom). The coloured and black lines correspond to the observed and calculated intensities, respectively. Incident light wavelengths of $\lambda = 1.5405 \text{ \AA}$ and 0.43046 \AA were used for the room- and low-temperature measurements, respectively. The high-resolution XRD data are consistent with the $I-4m2$ symmetry and confirm the tetragonal crystal structure at low temperatures.

tained using a Guinier camera ($\text{Cu K}\alpha$ radiation) with LaB_6 acting as the internal standard. The samples were first sieved through a $40 \text{ }\mu\text{m}$ mesh. Rietveld refinement was performed using the FullProf software [1] for the structure analysis.

In the case of Mn_2RhSn [2], low-temperature X-ray diffraction patterns were measured at ESRF, Grenoble, with an incident beam wavelength of 0.43046 \AA for a high-resolution data analysis. The Mn_2RhSn compound crystallizes in an inverse tetragonal 119 Heusler structure (with Wyckoff sites of Mn_I : $(0, 0, \frac{1}{2})$; Mn_II : $(0, \frac{1}{2}, \frac{1}{4})$; Rh: $(0, \frac{1}{2}, \frac{3}{4})$; and Sn: $(0, 0, 0)$). Mn_2IrSn and Mn_2PtIn [3] crystallize in the same structure with lattice parameters

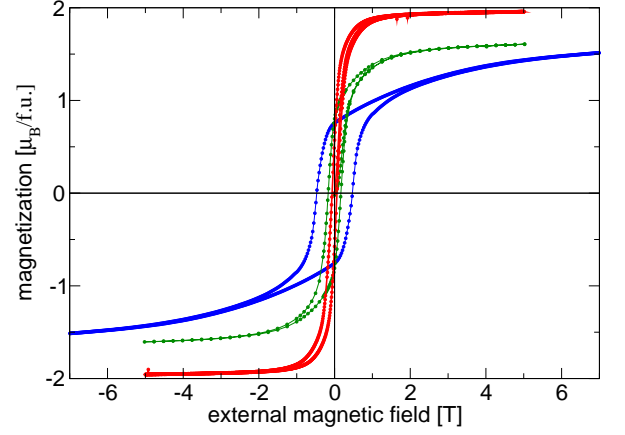


FIG. S4. Magnetic hysteresis loops measured at 1.8 K of polycrystalline Mn_2RhSn [2] (red), Mn_2PtIn [3] (green), and Mn_2IrSn (blue; present work) samples.

of $a = 4.29 \text{ \AA}$, $c = 6.59 \text{ \AA}$ and $a = 4.32 \text{ \AA}$, $c = 6.77 \text{ \AA}$, respectively.

B. Magnetic and thermal measurements

Magnetization measurements were performed in constant field sweeps at different temperatures using the Quantum Design MPMS XL superconducting quantum interference device (SQUID) magnetometer. The total magnetization was obtained from the hysteresis loop at 1.8 K (Fig. S4) and was $1.97 \mu_B$ (per formula unit). In the zero-field-cooled (ZFC) mode, the sample was initially cooled in the absence of a field down to 2 K, and data were collected as the temperature was increased in the applied field. In the field-cooled (FC) mode, data were collected while the sample was cooled in the field, and subsequently, data were also collected while the sample was heated in the field during the field-heated (FH) mode. The real (χ') and imaginary (χ'') parts of the ac-susceptibility were obtained simultaneously at the lowest possible dc-field of 50 Oe. Various field frequencies from 33 to 9997 GHz were applied over the temperature range of 2 to 300 K. The heat capacity measurements were performed in zero field over the same temperature range. A transition to the high-temperature cubic phase (Fig. S5) was observed with the help of differential scanning calorimetry (DSC) at a moderate rate of 10 K/min; the powder sample was encapsulated in an Al_2O_3 crucible and measured in an Ar atmosphere.

III. NEUTRON SCATTERING

A two-axis diffractometer equipped with a vertical focusing pyrolytic graphite monochromator and a cold neutron guide was used for the neutron scattering measurements. The sample was encapsulated in a vana-

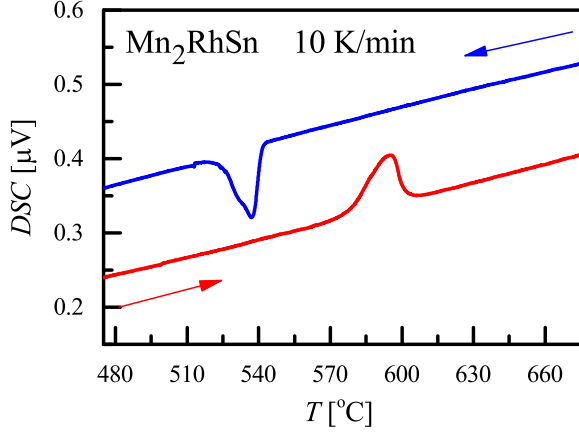


FIG. S5. The transition from the high-temperature cubic to low-temperature tetragonal phase occurs between 537 and 594°C. Red and blue curves correspond to the heating and cooling regimes, respectively.

Mn _I [μ_B]	Mn _{II} [μ_B]	θ [°]	a [Å]	c [Å]
$M_z = M_{\text{tot}}$	M_x M_z	M_{tot}		
3.59	2.10 -1.80	3.47	58.9	4.261 6.261

TABLE S2. Refined values of the powder Mn₂RhSn sample obtained from neutron scattering measurements.

dium crucible, and the sample environment was constant throughout the measurement. The magnetic and nuclear structures were refined by the Rietveld method using the FullProf software [1]. The nuclear phase was first optimized above the magnetic ordering temperature, and the obtained parameters were later used for the refinement of the magnetic phase. This significantly improved the sigma deviations and R factors. The background was modelled by interpolation between manually selected points. The peak shape profile was described by a pseudo-Voigt function with a refined ratio between the Gaussian and Lorentzian contributions. Different oxidation states, Mn_I³⁺ and Mn_{II}²⁺, were assumed to calculate the magnetic scattering form factors. The results of the neutron scattering measurements are listed in Tab. S2.

Several refinement approaches were used by fixing or releasing certain, all, or some parameters. In total, we varied 10 parameters: the scale, zero-shift, a -constant, c -constant, projections of the spin [M_z (Mn_I), M_x (Mn_{II}), and M_z (Mn_{II})], Lorentzian-to-Gaussian ratio in the peak shape (varied separately for the Bragg and magnetic phase), and overall isotropic displacement (temperature) factor. The room-temperature pattern was refined first to eliminate any contribution of the magnetic signal, and the obtained zero-shift value was then fixed to avoid errors in the lattice parameters.

The lattice constants are robust and independent of the specific refinement procedure. We also found that the Mn_I moment was indeed strongly localized and aligned along the crystallographic z -axis. If a slight deviation

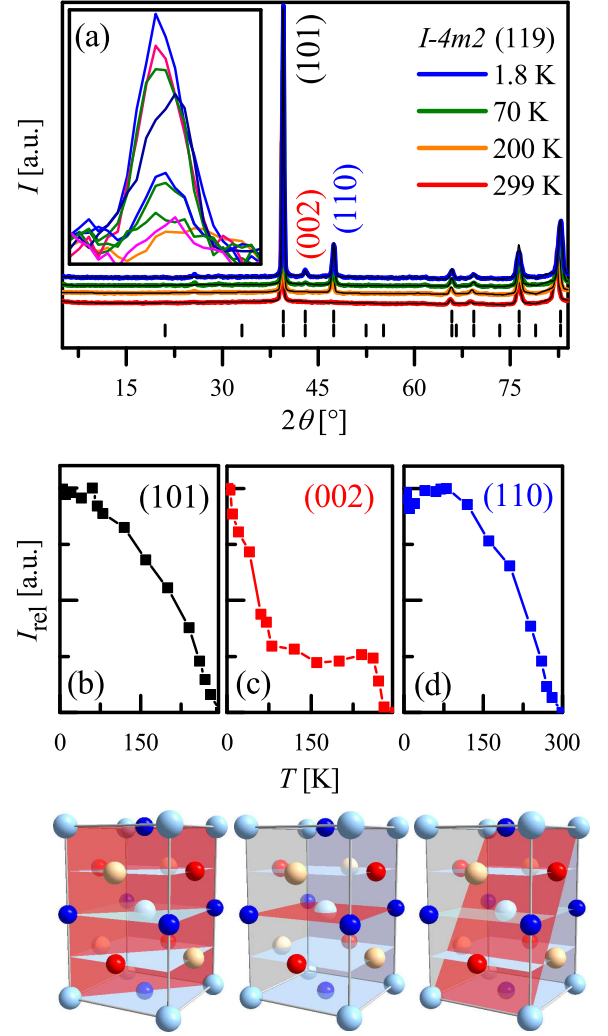


FIG. S6. Neutron data of Mn₂RhSn. (a) Evolution of the neutron spectra with temperature (1.8 K, 70 K, 200 K and 299 K); peak positions from the Bragg and magnetic phases are distinguished by vertical markers. Inset: evolution of (002) peak within the whole temperature regime. Normalized intensity of the (101), (002) and (110) peaks ((b), (c), (d) panels, respectively) together with the corresponding crystal planes.

from this direction is introduced, then the refinement does not converge. In contrast, the Mn_{II} moment prefers a canted orientation, and the obtained absolute value of the Mn_{II} moment was slightly higher than that predicted theoretically: 3.47 μ_B as opposed to 3.08 μ_B . The value of the Mn_I moment, however, was in good agreement with the predicted value: 3.59 μ_B to 3.51 μ_B .

The magnetic state appears to be well-analyzable due to its noticeable contribution to the overall intensity: e.g., (101)-peak increases by nearly 65% with temperature decrease from $T = 299$ K (paramagnetic) to 1.8 K. The additional intensity contains only that magnetic component, which is perpendicular to the scattering vector; therefore the neutrons reflected from the (101), (002) and (110) crystal planes give us an estimate how the mag-

netic moment evolves within these planes (see Fig. S6). For $T > 80$ K the magnetic contribution to the (002) peak vanishes and only the Bragg intensity is observed. The in-plane magnetism is realized by canting of the Mn_{II} moment.

IV. DISORDER EFFECTS AND THE PHASE STABILITY OF Mn_2RhSn

Chemical disorder, which often occurs in multicomponent systems, such as Heusler alloys, may severely influence the magnetic properties. Random exchange between Rh and Mn_{I} would increase the amount of Mn_{II} type (magnetically antiparallel to Mn_{I}). In turn, the exchange between Sn and Mn_{II} will increase the amount of Mn_{I} type. The exchange between Rh and Sn will locally convert Mn_{I} into Mn_{II} within Mn_{I} -Sn planes, and Mn_{II} into Mn_{I} within Mn_{II} -Rh planes. In which way particular type of disorder will affect the system exactly, is rather complicated question, as it implies not just a straightforward redistribution of different Mn types, but the change of the whole magnetic coupling picture. It is easy to show (e.g., by first-principle calculations) that in all cases the total energy drastically increases, which indicates that such events are of small probability (once the system holds the correct stoichiometry and is properly annealed). In any case, if such situation would occur, the interpretation of the neutron spectra using the proposed magnetic picture would be unreliable.

For the present samples such straightforward reason for chemical disorder as deviation between the actual and the target compositions can be excluded due to the high quality evidenced by EDX and also XRD (see Fig. S2, Tab. S1). Within this restriction, certain random intermixing of different atomic types would be still possible. However, any mixtures involving Sn are unlikely, as it affects the zinc-blende sub-structure, which is the “skeleton” of any Heusler alloy (as one can represent the Heusler system as zinc-blende plus extra transition element). Certain intermixing within Rh- Mn_{II} plane would still be possible (indeed, there are Heusler systems stabilized by such mechanisms, e.g. Fe_2CuGa which exhibits Fe-Cu intermixing [4]). However such disorder at high rates would lead to the statistical emergence of the inversion symmetry, which contradicts to the present XRD data (Fig. S7), convincingly deducing the noncentrosymmetric group $I-4m2$ (No. 119) instead of $I4/mmm$ (No. 139).

Experimentally the compositional stability of the compound was investigated by considering Mn- and Rh-excess regimes. The Mn-excess series ($\text{Mn}_{3-x}\text{Rh}_x\text{Sn}$, with the composition step of 0.1) always exhibit the phase separation in a form of a growing amount of Mn-rich Mn_3Sn phase (group No. 194, hexagonal) and the “host” phase of Mn_2RhSn . There is no direct transition between these crystal structures for the symmetry reasons: right at $\text{Mn}_{2.1}\text{Rh}_{0.9}\text{Sn}$ composition the phase separation

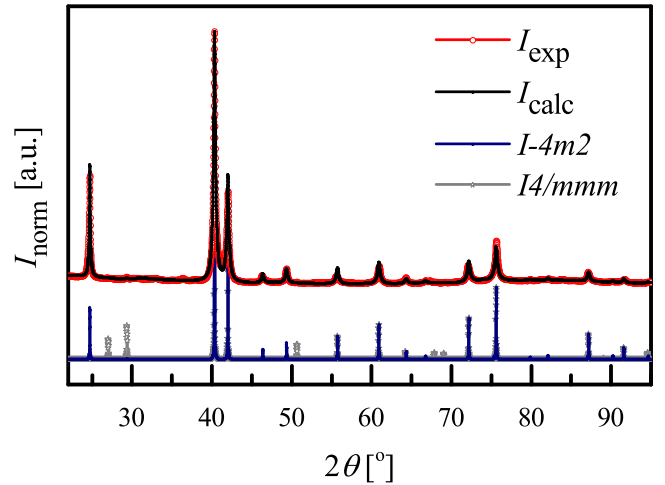


FIG. S7. XRD powder pattern (red) of Mn_2RhSn . The measured pattern has been refined using the noncentrosymmetric tetragonal Heusler structure $I-4m2$ (No. 119) as a model. For comparison, both $I-4m2$ (119) and $I4/mmm$ (139) structures are showed below (blue and gray, respectively).

sets in, as observed with the help of XRD, EDX, optical and electron microscopy. Introduction of additional Rh in Mn_2RhSn system reduces the c/a ratio and gradually brings the structure to the cubic phase. The smallest Rh content, which is enough to form a cubic structure is $\text{Mn}_2\text{Rh}_{1.17}\text{Sn}$. Thus, the Mn_2RhSn phase is rather sensitive to a slight stoichiometric deviation of Rh or Mn. For the working composition (i.e., Mn_2RhSn) the Rietveld refinement of the 2:1:1 sample shows the R -Bragg factor of 3.998. If present, the disorder between Mn and Rh atoms would contribute additional intensities to (002), (110), (202) and (310) peaks whereas the (101), (103), (211), (301), (321) and (215) would be suppressed (see Fig. S7)

V. COMPUTATIONAL DETAILS

To justify the proposed magnetic order, first-principles calculations using the spin-polarized relativistic Korringa-Kohn-Rostoker (SPR-KKR) Green’s function method [5] within a local density approximation [6] were performed for several Mn_2YZ Heusler materials: the recently synthesized Mn_2PtIn [3], Mn_2RhSn [2], and Mn_2IrSn , which is reported for the first time in the present work. To determine the magnetic ground states, we started with the experimental lattice parameters and allowed for the self-consistent determination of local moments including their amplitudes, directions, and periodicity.

From the total energies obtained as a function of θ (Fig. S8), not only both the Sn-containing compounds but also the In-containing compound exhibit noncollinear magnetic order characterized by canting of the Mn_{II} local moment direction: $\theta_{1,2} = 180^\circ \pm 55^\circ$, $180^\circ \pm 50^\circ$, and

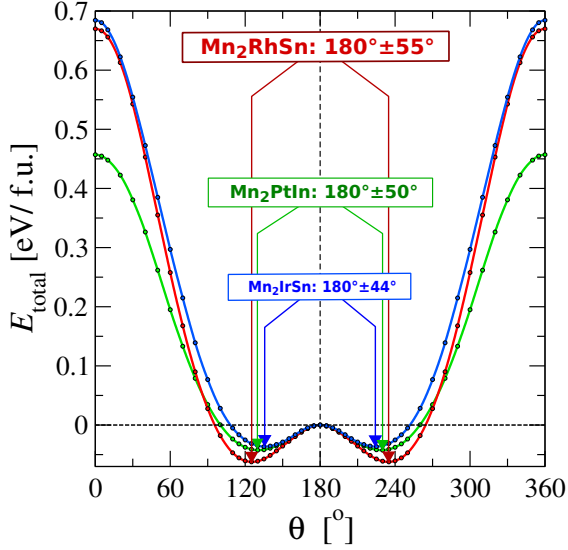


FIG. S8. Total energy per formula unit computed as a function of the orientation of the Mn_{II} magnetic moment characterized by angle θ . The energy minima (indicated by arrows) occur at $\theta_{1,2} = 180^\circ \pm 55^\circ$, $180^\circ \pm 50^\circ$, and $180^\circ \pm 44^\circ$ in the case of Mn_2RhSn , Mn_2PtIn , and Mn_2IrSn , indicated respectively by red, green, and blue.

$180^\circ \pm 44^\circ$ for Mn_2RhSn , Mn_2PtIn and Mn_2IrSn , respectively. Upon closer examination of Fig. S8, the largest energy scale (~ 0.67 , 0.45 , and 0.6 eV for Mn_2RhSn , Mn_2PtIn , and Mn_2IrSn , respectively) is revealed to be the difference between two collinear configurations: the FM (ferromagnetic, $\theta = 0^\circ$) and FiM (ferrimagnetic, $\theta = 180^\circ$) configuration. Thus, the small energy (0.06 , 0.04 , and 0.09 eV for Mn_2RhSn , Mn_2PtIn , and Mn_2IrSn , respectively) gained by canting can be considered as a perturbation of the collinear ferrimagnetic state, which is typical for most Mn_2 -based Heusler systems.

To ensure that the canted magnetic state that is obtained is due to the proposed mechanism, we computed the exchange coupling constants (using the approach in Ref. [7]) for the model Eq. (1, 3) and calculated the canting directly from minimizing the Heisenberg Hamiltonian (1). For example, the values obtained for Mn_2RhSn ($J = -63.46$ and $j = -53.05$ meV) satisfy criterion (2): $j/J = 0.83 > 1/2$. This then leads to $\theta_{1,2} = 180^\circ \pm 53.3^\circ$, which is in reasonable agreement with the *ab initio* calculated value in Tab. I (in the main part). The same holds also for the In-based compound Mn_2PtIn : $J = -36.64$ and $j = -27.67$ meV gives $j/J = 0.75 > 1/2$, leading to $\theta_{1,2} = 180^\circ \pm 48.6^\circ$.

In order to analyze the possible long-range magnetic orders, and in particular, the possibility of skyrmions in Mn_2RhSn , we computed the absolute values of the Dzyaloshinskii-Moriya (DM) vectors for Mn_2RhSn , by following the scheme introduced in Ref. [8]. In addition we computed the magnetocrystalline anisotropy as the energy difference between orientations of the total magnetization along the c -axis and within ab -plane. Due to

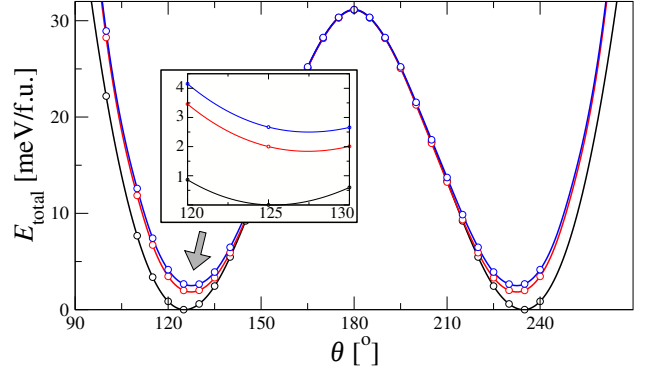


FIG. S9. Total energy per Mn_2RhSn formula unit computed as a function of the orientation of the Mn_{II} magnetic moment characterized by angle θ . We compare three magnetic orientations: black - total magnetization is along the c -axis; blue and red - total magnetization within ab -plane, but with Mn_{II} -moments staggering within ab and within ac -planes, respectively. Inset shows the detailed energy trends near the canting minimum at about 125° .

canting, for the second case we distinguish two orientations - first, when Mn_{II} moments stagger within ab -plane and second - within ac -plane (see Fig. S9). As it follows from the inset, the energy minima for the ab -orientations are shifted by few degrees. Their absolute values are about 2.5 (staggering within ab -plane) and 1.8 meV/f.u. (staggering within ac -plane).

VI. CONTINUUM MODEL OF MAGNETIC ORDER IN Mn_2RhSn

The phenomenological continuum theory for the magnetism of Mn_2RhSn can be written in terms of the four sublattices ($l = 1, 2, 3, 4$) consisting of the two sublattices Mn_{I} on Wyckoff site $2a$ and Mn_{II} on site $2c$. We use standard methods to derive a quantitative model in the shape of this phenomenological theory by a systematic coarse graining of a microscopic model, where direct and antisymmetric DM exchange are calculated with DFT methods (discussed in previous section). Eventually, by adding magnetic anisotropies, also from DFT calculations and Zeeman energy, a micromagnetic low-temperature continuum model can be constructed. For the thermal phase diagram, empirical input is needed to write a Landau-Ginzburg functional for coupled magnetic modes. As the low acentric symmetry of Mn_2RhSn allows for the presence of chiral inhomogeneous DM couplings, the resulting model has the form of a Dzyaloshinskii-model [9] marked by the presence of Lifshitz-type invariants that couple different magnetic order parameters.

The magnetic moments \mathbf{S}_l in each unit cell of the lattice \mathbf{R}_n , $\mathbf{n} = (i, j, k)$ of each sublattice are expressed by a continuous functions $\mathbf{m}_l(\mathbf{r})$ with the property

$$\mathbf{m}_l(\mathbf{R}_n + \mathbf{b}_l) = \mathbf{S}_l(\mathbf{R}_n), \quad (1)$$

where \mathbf{b}_l are the base vectors of the sublattice sites.

The magnetic free energy is expressed by a standard gradient expansion up to square terms,

$$w = \sum_{l,m} \sum_{\alpha\beta} A_{lm}^{\alpha\beta} \partial_\alpha \mathbf{m}_l \cdot \partial_\beta \mathbf{m}_m + \sum_{\gamma} \sum_{l,m} \sum_{\alpha\beta} D_{lm}^{(\gamma)\alpha\beta} m_l^\alpha \bar{\partial}_\gamma m_m^\beta + w_1(\{\mathbf{m}_l\}). \quad (2)$$

The first two lines describe the inhomogeneous exchange by a set of (anisotropic) constants $A_{lm}^{\alpha\beta}$, where $\alpha\beta$ are labels of Cartesian coordinates, and the second line gives the inhomogeneous DM couplings $D_{lm}^{(\gamma)\alpha\beta}$ that arise in low symmetry crystals. The Lifshitz-type invariants are written in short form, $a\bar{\partial}b \equiv a\partial b - b\partial a$. Finally w_1 collects the terms which are homogeneous in the set of functions $\{\mathbf{m}_l\}$. Within our ansatz this contribution can be written as $w_1 = w_0 + w_a + w_h \dots$, where w_0 collects contributions deriving from isotropic exchange only, and w_a, w_h contains anisotropic and Zeeman terms, including the demagnetization energy.

This coarse grained continuum theory for the ground-state can be derived from the microscopic classical Hamiltonian of the lattice and symmetry constraints. Using the results of the *ab initio* calculations the magnetic energy can be expressed by a model including direct (isotropic) Heisenberg-like exchange couplings and the DM-couplings:

$$H = -\frac{1}{2} \sum_{\mathbf{n}} \sum_{\mathbf{p}} \sum_{lm} J_{lm}(\mathbf{R}_{\mathbf{p}} - \mathbf{R}_{\mathbf{n}}) \mathbf{S}_l(\mathbf{R}_{\mathbf{n}}) \cdot \mathbf{S}_m(\mathbf{R}_{\mathbf{p}}) + \sum_{\mathbf{n}} \sum_{\mathbf{p}} \sum_{lm} \mathbf{D}_{lm}(\mathbf{R}_{\mathbf{p}} - \mathbf{R}_{\mathbf{n}}) \cdot (\mathbf{S}_l(\mathbf{R}_{\mathbf{n}}) \times \mathbf{S}_m(\mathbf{R}_{\mathbf{p}})). \quad (3)$$

Expanding the continuous functions for the sublattices into a Taylor series,

$$\mathbf{m}_l(\mathbf{r}_0 - \mathbf{r}) = \mathbf{m}_l(\mathbf{r}_0) + \sum_{\nu} \frac{1}{\nu!} [(\mathbf{r} - \mathbf{r}_0) \cdot \nabla]^\nu \mathbf{m}_l(\mathbf{r}_0), \quad (4)$$

and using Eq.(1) in this Heisenberg-DM-Hamiltonian, the continuum theory can be derived. For Mn_2RhSn with the tetragonal lattice described by space group $I\bar{4}m2$ crystal class $\bar{4}m2$ (D_{2d}), the effective model simplifies to

$$w = \sum_{lm} \sum_{x=a,b,c} A_{lm}^x \sum_{\alpha} (\partial_x m_l^\alpha \partial_x m_m^\alpha) + \sum_{lm} [D_{lm}^a m_l^z \bar{\partial}_a m_m^b + D_{lm}^b m_l^z \bar{\partial}_b m_m^a] + \sum_{lm} J_{lm} \mathbf{m}_l \cdot \mathbf{m}_m, \quad (5)$$

where the surface terms and constants have been omitted. The gradients $\partial_a, \partial_b, \partial_d$ are written along and in units of the tetragonal lattice cell. The coefficients J_{lm} (Tab. S3),

$l \backslash m$	1	2	3	4
1	7.5	-10.4	4.1	-10.3
2	-10.4	21.3	-10.3	-27.2
3	4.1	-10.3	7.5	-10.4
4	-10.3	-27.2	-10.4	21.3

TABLE S3. Coefficients of the effective homogeneous exchange J_{lm} [meV/ μ_B^2].

$l \backslash m$	A^a				A^b				A^c			
	1	2	3	4	1	2	3	4	1	2	3	4
1	5.0	5.1	-0.4	-1.3	4.9	-1.4	-0.4	5.2	0.8	2.5	1.0	2.6
2	5.1	21.2	-1.3	-2.4	-1.4	21.2	5.2	-2.5	2.5	7.9	2.6	-6.8
3	-0.4	-1.3	5.0	5.1	-0.4	5.2	4.9	-1.4	1.0	2.6	0.8	2.5
4	-1.3	-2.4	5.1	21.2	5.2	-2.5	-1.4	21.2	2.6	-6.8	2.5	7.9

TABLE S4. Coefficients of the inhomogeneous exchange $A_{lm}^{a,b,c}$ [meV/ $(\mu_B^2 a^2)$].

$l \backslash m$	D^a				D^b			
	1	2	3	4	1	2	3	4
1	-0.34	0.04	-0.47	-0.49	-0.34	-0.49	-0.47	0.04
2	0.00	0.64	-0.49	0.21	0.00	0.64	0.04	0.21
3	-0.47	-0.49	-0.34	0.04	-0.47	0.04	-0.34	-0.49
4	-0.49	0.21	0.04	0.64	0.04	0.21	-0.49	0.64

TABLE S5. Coefficients of the inhomogeneous DM-exchange $D_{lm}^{a,b}$ [meV/ $(\mu_B^2 a)$].

A_{lm}^x (Tab. S4), D_{lm}^x (Tab. S5), now describe effective coarse grained exchange and DM-couplings.

It must be noted that there is no weak ferromagnetism or weak antiferromagnetism in the tetragonal inverse Heusler structure, i.e., there are no bilinear coupling terms between components of the staggered and ferromagnetic vectors derived from the DM-exchange, because the four sublattices are related by non-primitive translations. After quantification of the exchange couplings terms, it is convenient to analyse the 4-sublattice system by using staggered and ferromagnetic vectors of two sublattices,

$$m_{\text{MnI}} \cdot \mathbf{L} = \frac{(\mathbf{m}_1 - \mathbf{m}_3)}{2}; \quad m_{\text{MnI}} \cdot \mathbf{F} = \frac{(\mathbf{m}_1 + \mathbf{m}_3)}{2}; \quad (6)$$

$$m_{\text{MnII}} \cdot \mathbf{l} = \frac{(\mathbf{m}_2 - \mathbf{m}_4)}{2}; \quad m_{\text{MnII}} \cdot \mathbf{f} = \frac{(\mathbf{m}_2 + \mathbf{m}_4)}{2},$$

where the spin vectors \mathbf{L} and \mathbf{F} are related to MnI , and \mathbf{l} and \mathbf{f} – to MnII sublattice. In the ground-state configurations, these vectors fulfill

$$\begin{aligned} \mathbf{L}^2 + \mathbf{F}^2 &= 1; & \mathbf{L} \cdot \mathbf{F} &= 0 \\ \mathbf{l}^2 + \mathbf{f}^2 &= 1; & \mathbf{l} \cdot \mathbf{f} &= 0. \end{aligned} \quad (7)$$

Dropping irrelevant terms, the homogeneous part of the

continuum theory now is expressed as

$$\begin{aligned}\tilde{w}_0 = & J_F \mathbf{F} \cdot \mathbf{F} + J_L \mathbf{L} \cdot \mathbf{L} + J_f \mathbf{f} \cdot \mathbf{f} + J_l \mathbf{l} \cdot \mathbf{l} \\ & + J_c \mathbf{F} \cdot \mathbf{f} + J' \mathbf{F} \cdot \mathbf{l} \\ & - 2(m_{\text{MnI}} \cdot \mathbf{F} + m_{\text{MnII}} \cdot \mathbf{f}) \cdot \mathbf{H},\end{aligned}\quad (8)$$

with coefficients in [meV]:

J_F	J_L	J_f	J_l	J_c	J_{Ff}	J_{Fl}	J_{Lf}	J'	J_{Ll}
-285.4	-83.1	111.3	-920.0	898.2	898.2	0	0	4.8	4.8

Here we use an obvious notation for the effective exchange, internal to the ordering modes and between the modes, and using the spin moments from the DFT calculations $m_{\text{MnI(II)}} = 3.51$ (3.08) μ_B (see Sec. V). The field \mathbf{H} in (8) is the internal magnetic field. It is seen that the exchange couplings have a clear hierarchy, showing that magnetic ordering is either dominated by the FM order on MnI sublattice or by staggered AFM order on MnII . This AFM order is only very weakly coupled via the staggered vectors \mathbf{L} , which however is not the dominating magnetic mode on MnI sublattice. Hence, Mn_2RhSn is close to a tetracritical (or bicritical) point, where these two magnetic modes would coexist with the paramagnetic state. The FM mode \mathbf{f} is a secondary magnetic order for sublattice MnII , which is *antiparallel* to \mathbf{F} via the very strong coupling J_c . The superposition of \mathbf{F} , \mathbf{l} and \mathbf{f} determines a canted state for the magnetic order with the magnetic cell equivalent to the crystallographic unit cell, i.e. a Γ -point mode.

Ground state. The homogeneous ground state can be found by neglecting in (8) the small coupling J' , and writing a coplanar canted state arbitrarily in the ac -plane, using $\mathbf{F} \equiv \mathbf{F}_0 = (0, 0, 1)$, $\mathbf{l} \equiv \mathbf{l}_0 = (\sin[\pi - \vartheta], 0, 0)$, and $\mathbf{f} \equiv \mathbf{f} = (0, 0, \cos[\pi - \vartheta])$. Its energy is given by

$$w_0 = J_F + J_l + (J_f - J_l) \xi^2 + J_c \xi; \quad \xi = \cos[\pi - \vartheta]. \quad (9)$$

The solution for the canting angle is

$$\vartheta = \pi - \arccos \frac{J_c}{2(J_f - J_l)}. \quad (10)$$

Using the parameters above, the canting angle is $\vartheta_0 = 64.2^\circ$, which is in reasonable agreement with the *ab initio* calculations finding $\theta_{1,2} = 55^\circ$, considering that the exchange approximation in Eq. (8) neglects the anisotropy which has an easy-axis character for the canted sublattice MnII (see Fig. S9). The ground state, thus, is composed of the two modes \mathbf{F} and \mathbf{l} , which are almost decoupled for $J' \simeq 0$, and by the induced FM mode \mathbf{f} on MnII . However, the conditions (7) provide a non-linear coupling between these different modes in a proper micromagnetic model.

Inhomogeneous states. The micromagnetic model requires now to include the exchange terms and the inhomogeneous DM-couplings, i.e., the gradient energy is given by

$$w_2 = w_J + w_D, \quad (11)$$

where we have the squared gradient terms derived from the isotropic exchange in the form

$$\begin{aligned}w_J = & A_F^\perp [\partial_a \mathbf{F} \cdot \partial_a \mathbf{F} + \partial_b \mathbf{F} \cdot \partial_b \mathbf{F}] + A_F^\parallel \partial_c \mathbf{F} \cdot \partial_c \mathbf{F} \\ & + A_l^\perp [\partial_a \mathbf{l} \cdot \partial_a \mathbf{l} + \partial_b \mathbf{l} \cdot \partial_b \mathbf{l}] + A_l^\parallel \partial_c \mathbf{l} \cdot \partial_c \mathbf{l} \\ & + A_f^\perp [\partial_a \mathbf{f} \cdot \partial_a \mathbf{f} + \partial_b \mathbf{f} \cdot \partial_b \mathbf{f}] + A_f^\parallel \partial_c \mathbf{f} \cdot \partial_c \mathbf{f} \\ & + A_{Ff}^\perp [\partial_a \mathbf{F} \cdot \partial_a \mathbf{f} + \partial_b \mathbf{F} \cdot \partial_b \mathbf{f}] + A_{Ff}^\parallel \partial_c \mathbf{F} \cdot \partial_c \mathbf{f}\end{aligned}\quad (12)$$

with coefficients in [meV/ a^2] units:

A_F^\perp	A_F^\parallel	A_l^\perp	A_l^\parallel	A_f^\perp	A_f^\parallel	A_{Ff}^\perp	A_{Ff}^\parallel	A_{Fl}^\perp	A_{Fl}^\parallel
9.25	3.61	37.50	2.23	47.30	29.40	15.11	20.33	$\simeq 0$	$\simeq 0$

The inhomogeneous DM-couplings are

$$\begin{aligned}w_D = & D_F [F^c \bar{\partial}_b F^a + F^c \bar{\partial}_a F^b] \\ & + D_l [l^c \bar{\partial}_b l^a + l^c \bar{\partial}_a l^b] \\ & + D_f [f^c \bar{\partial}_b f^a + l^c \bar{\partial}_a f^b] \\ & + D_c [F^c \bar{\partial}_b f^a + F^c \bar{\partial}_a f^b + f^c \bar{\partial}_b F^a + f^c \bar{\partial}_a F^b],\end{aligned}\quad (13)$$

with coefficients in [meV/ a] units:

D_F	D_l	D_f	D_c
-9.8	5.1	7.0	-9.8

An inhomogeneous modification of the ground-state takes place on long lengths, owing to the weakness of the DM-exchange compared to the direct exchange. Considering that the DM-couplings and also applied magnetic fields and anisotropies are small in comparison to the strong local exchange forces, the basic canted structure is preserved in each unit cell. But it can be slowly rotated over length of many unit cells.

Landau-Ginzburg functional. In order to complete the phenomenological theory, we briefly discuss the form of an appropriate Landau-Ginzburg functional which could be used to model the thermal phase diagram and the phase transitions. The two primary order parameters (OPs) are the FiM and the AFM modes, \mathbf{F} and \mathbf{l} . They and the coupling between them have to be considered with respect to the secondary OP, which is the FM mode \mathbf{f} . The complete Landau-Ginzburg (LG) functional contains Lifshitz invariants w_D from Eqs. (13). Hence, this LG-functional is not a simple extension of a proper Landau-theory with the set of applicable squared-gradient terms w_J from (12), as the magnetic free energy violates the Lifshitz condition. Consequently, this *Dzyaloshinskii model* should be understood as a pseudo-microscopic continuum theory. Still, the LG functional for Mn_2RhSn can be written by using standard Landau expansion for the homogeneous coupling terms, instead

of \tilde{w}_0 :

$$\begin{aligned}
w_0 = & a_F \mathbf{F} \cdot \mathbf{F} + b_F (\mathbf{F} \cdot \mathbf{F})^2 \\
& + a_l \mathbf{l} \cdot \mathbf{l} + b_f (\mathbf{l} \cdot \mathbf{l})^2 \\
& + a_f \mathbf{f} \cdot \mathbf{f} \\
& + c_f \mathbf{F} \cdot \mathbf{f} + c' \mathbf{F} \cdot \mathbf{l} \\
& + b_{Ff} |\mathbf{F}|^2 |\mathbf{f}|^2 + b_{Fl} |\mathbf{F}|^2 |\mathbf{l}|^2 + b_{fl} |\mathbf{f}|^2 |\mathbf{l}|^2 \\
& + b_c (\mathbf{F} \cdot \mathbf{f})^2 + b' (\mathbf{F} \cdot \mathbf{l})^2 \\
& + \text{h.o.t.} \\
& - 2(\mathbf{F} + \mathbf{f}) \cdot \mathbf{H},
\end{aligned} \tag{14}$$

where all magnetizations \mathbf{F} , \mathbf{f} , and \mathbf{l} are now considered as variable length 3-component vectors. The complete LG functional for the magnetic free energy then is given by

$$w_{LG} = w_0 + w_J + w_D + w_a, \tag{15}$$

where the w_a collects anisotropic contributions, not contained in the first three terms, i.e., the magnetocrystalline and exchange anisotropies.

A complete microscopic derivation of the terms in the LG-functional would require a detailed finite temperature statistical theory beyond the input from the DFT-calculations for ground-states. And, for the behavior at lower temperatures, the higher-order-terms (h.o.t.'s) are required in the thermodynamic potential. However, a semi-quantitative model could be written in the usual manner by restricting the temperature dependence of the model to the coefficients of the square terms in the primary OPs:

$$\begin{aligned}
a_F(T) &= \alpha_F (T - T_C^0) \\
a_l(T) &= \alpha_l (T - T_N^0)
\end{aligned} \tag{16}$$

In Mn_2RhSn the bare FiM Curie-temperature $T_C^0 \sim 280 \text{ K} < T_C$, and the $T_N^0 \sim 80 \text{ K}$, i.e. close to the onset of the AFM mode on Mn_{II} -sublattice. These bare or ideal transition temperatures should not deviate strongly from the observed magnetic transition temperatures, because the corrections due to DM-exchange [10] and anisotropy are expected to remain small. Magnitude of the remaining coefficients a_f and of the quartic terms with coefficients b_ν could roughly be fixed to the empirical ordered moments. Here, we only note that the suppression of the FM mode \mathbf{F} on Mn_{I} -sublattice below the onset of the AFM signals, a bicritical behavior with a repulsive interaction, i.e. $b_{Fl} > 0$, while b_{fl} may be small. This suggests that the thermal magnetic phase diagram of Mn_2RhSn is close to a *bicritical* behavior, where the FiM and AFM modes rather compete and inhomogeneous textures can occur.

Skyrmions in the ferrimagnetic state. The qualitative discussion of the LG-functional is sufficient to understand the basic features of inhomogeneous state in the intermediate temperature range $T_N^0 < T < T_C$ where only the FiM collinear state exists. In that case, the FM mode on the Mn_{II} -sublattice is antiparallel to FM mode on the

Mn_{I} -sublattice, $\mathbf{f} = -\mathbf{F}$. Inserting this into $w_J + w_D$ in Eqs. (12)-(13) and adding Zeeman term an magnetocrystalline uniaxial anisotropy yields a functional describing inhomogeneous FiM states in the ab -plane :

$$\begin{aligned}
\tilde{w}_{\text{FiM}} = & \tilde{A} [\partial_a \mathbf{F} \cdot \partial_a \mathbf{F} + \partial_b \mathbf{F} \cdot \partial_b \mathbf{F}] \\
& + \tilde{D} [F^c \bar{\partial}_b F^a + F^c \bar{\partial}_a F^b] \\
& - 2(m_{\text{MnI}} - m_{\text{MnII}}) \mathbf{F} \cdot \mathbf{H} \\
& - K (F^c)^2.
\end{aligned} \tag{17}$$

This free-energy functional for the FiM state is exactly equivalent to the FM Dzyaloshinskii-model for chiral magnets from crystal class $\bar{4}2m$ studied earlier [11, 12]. In particular, the solutions for isolated and condensed chiral “vortices” and the magnetic phase diagram presented in this pioneering work describe what is now known as chiral skyrmions in the FiM state of acentric Mn_2YZ inverse tetragonal Heusler alloys.

The parameters of this model for Mn_2RhSn can be calculated from the microscopic input as $\tilde{A} = A_F + A_f - 2A_{Ff} = 16.5 \text{ [meV/\text{\AA}^2]}$ and $\tilde{D} = D_F + D_f - D_c = 7.0 \text{ [meV/\text{\AA}]}$. The DFT calculations of anisotropy (see Sec. V) suggest an effective easy-axis anisotropy of the order $K \simeq 2 \text{ [meV/f.u.]}$. We may assume that the magnetic coupling coefficients do not depend strongly on temperature, i.e. their temperature dependence should essentially scale only with the square of the saturation magnetization. This means that all the ratios of coupling terms in the free energy Eq. (17) are almost constant with temperature. Then, we may use the coefficients from the microscopic ground-state calculation to estimate materials parameters of Mn_2RhSn at elevated temperatures and evaluate the sizes or stability of skyrmions and the phase diagram in Mn_2RhSn in the FiM state. The chiral magnetic twisting lengths is given by

$$\Lambda = 4\pi \tilde{A} / \tilde{D}, \tag{18}$$

which means $\Lambda \sim 29.5 \text{ \AA} \sim 130 \text{ nm}$ for Mn_2RhSn . The strengths of the easy-axis anisotropy determines whether a modulated spiral ground-state exists and whether a field-induced skyrmion lattice in an effective field pointing along the c -axis occurs (see Figs. 9 and 10 in Ref. 12). The different cases can be distinguished by the parameter

$$\kappa = \pi \tilde{D} / 4 \sqrt{\tilde{A} K}. \tag{19}$$

For $\kappa < 1$, the ground state is collinear as the strong anisotropy suppresses the spiral state. For $\kappa > 1.14$, there is a field-induced skyrmion lattice in the magnetic equilibrium phase diagram for fields along c .

For the estimated coefficients, we find $\kappa \simeq 0.95$ as a reasonable value for Mn_2RhSn but close to the critical κ . The spiral magnetic states in crystals with $\bar{4}2m$ crystals can have demagnetizing fields, as they are of cycloidal (Néel)-like character when propagating along (110)-directions, while they are of helical (Bloch)-like

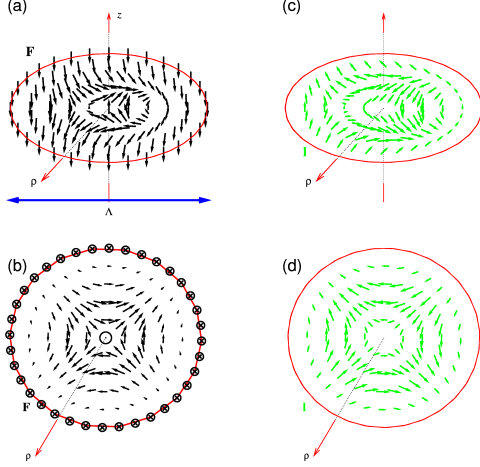


FIG. S10. (a) Shape of the double-twisted skyrmion configuration in the tetragonal inverse Heusler alloys of $\bar{4}2m$ symmetry. The FM magnetization \mathbf{F} on sublattice Mn_{I} parametrizes the FiM collinear state at higher temperatures in Mn_2RhSn . The corresponding magnetization \mathbf{f} on sublattice Mn_{II} is strictly antiparallel to \mathbf{F} . (b) Projection of the skyrmion in the ab -plane. (c) Close to the reorientation transition, the AFM mode \mathbf{l} on Mn_{II} -sublattice sets in: $|\mathbf{l}| \ll |\mathbf{F}|$ and also $|\mathbf{l}| \ll |\mathbf{f}|$. \mathbf{l} is perpendicular to \mathbf{F} and rotates with it in the same plane in each radial direction. In the center $|\mathbf{l}| = 0$. (d) Projection of \mathbf{l} onto ab -plane.

character for propagation along (100)-directions. The demagnetizing field further reduces the effective κ and oblique/skew spirals for propagation directions in between, as discussed in Ref. 12. Hence, the quantitative estimates for the micromagnetic model \tilde{w}_{FiM} suggest a collinear FiM state in Mn_2RhSn .

The solutions for isolated chiral skyrmions with a single FM ordering mode have been presented in Ref. 12 for the basic model Eqs. (17). The shape of an isolated skyrmion in Mn_2RhSn is sketched in Fig. S10. Close to the reorientation transition, where the AFM ordering sets in, the magnitude of the \mathbf{l} -mode is small and can be modulated ($|\mathbf{l}| \neq \text{const}$). As long this mode is subjugated to the FiM order it remains perpendicular to the \mathbf{F} -mode. Owing to its softness, it will not only rotate in a manner, so as to minimize the energy of its Lifshitz-invariants Eq. (13), it also will be modulated with a zero, $\mathbf{l} = 0$, in the center in form of a vortex-like defect. In Mn_2RhSn , the coefficients \bar{D} and D_l have similar magnitude and the same sign, so that the screw-sense of the rotation of \mathbf{F} and \mathbf{l} are not in conflict. Hence, close to T_N^0 the \mathbf{l} -mode follows and co-rotates the FiM mode \mathbf{F} while being modulated in lengths, Fig. S10 (c, d). At lower temperatures, the necessity to have a defect of the \mathbf{l} -mode in the skyrmion center and the associated large defect-energy most likely will destabilize the skyrmions. However, there may exist other localized solitonic textures in this acentric coupled magnetic system, which may cause inhomogeneous magnetic states to exist in the acentric Mn_2YZ alloys.

-
- [1] J. Rodríguez-Carvajal, *FULLPROF computer program*, LLB, Saclay (2004), version 2.80
 - [2] V. Alijani, O. Meshcheriakova, J. Winterlik, G. Kreiner, G. H. Fecher, and C. Felser, *J. Appl. Physics* **113**, 063904 (2013)
 - [3] A. K. Nayak, C. Shekhar, J. Winterlik, A. Gupta, and C. Felser, *Appl. Phys. Lett.* **100**, 152404 (2012)
 - [4] J. Kiss, S. Chadov, G. Fecher, and C. Felser, *Phys. Rev. B* **87**, 224403 (2013)
 - [5] H. Ebert, D. Ködderitzsch, and J. Minár, *Rep. Prog. Phys.* **74**, 096501 (2011)
 - [6] S. H. Vosko, L. Wilk, and M. Nusair, *Can. J. Phys.* **58**, 1200 (1980)
 - [7] A. I. Liechtenstein, M. I. Katsnelson, V. P. Antropov, and V. A. Gubanov, *J. Magn. Magn. Materials* **67**, 65 (1987)
 - [8] H. Ebert and S. Mankovsky, *Phys. Rev. B* **79**, 045209 (2009)
 - [9] I. E. Dzyaloshinskii, *Sov. Phys. JETP* **19**, 960 (1964)
 - [10] U. K. Rößler, A. N. Bogdanov, and C. Pfleiderer, *Nature* **442**, 797 (2006)
 - [11] A. N. Bogdanov and D. A. Yablonskii, *Sov. JETP* **68**, 101 (1989)
 - [12] A. N. Bogdanov and A. Hubert, *J. Magn. Magn. Materials* **138**, 255 (1994)